Available online at www.eccomasproceedia.org
Eccomas Proceedia COMPDYN (2017) 4796-4809

ECCOMAS
Proceedia

COMPDYN 2017
6th ECCOMAS Thematic Conference on
Computational Methods in Structural Dynamics and Earthquake Engineering
M. Papadrakakis, M. Fragiadakis (eds.)
Rhodes Island, Greece, 15–17 June, 2017

EXPERIMENTAL AND NUMERICAL STUDY OF WAVE DYNAMICS IN TENSEGRITY COLUMNS

Ada Amendola[1], Francesco Fabbrocino[2], Antonino Favata[3], Andrea Micheletti[4], Fernando Fraternali[1], Chiara Daraio[5]

[1]Department of Civil Engineering, University of Salerno
84084 Fisciano (SA), Italy
e-mail: {adamendola, f.fraternali}@unisa.it

[2] Pegaso University, Department of Engineering
80132 Naples, Italy
email: francesco.fabbrocino@unipegaso.it

[3] Department of Structural and Geotechnical Engineering
Sapienza University of Rome 00197 Rome, Italy
e-mail: antonino.favata@uniroma1.it

[4] Department of Civil Engineering and Computer Science Engineering
University of Rome Tor Vergata, 00133 Rome, Italy
fibers email: micheletti@ing.uniroma2it

[5] Engineering and Applied Science, California Institute of Technology
Pasadena, CA 91125, USA
e-mail: daraio@caltech.edu

Keywords: Tensegrity column, impulsive dynamics, 3D printing, experimental testing, stick-and-spring structure.

Abstract. *This work deals with the experimental testing and the numerical simulation of the impulsive dynamics of a tensegrity lattice. The analyzed system is a column made of ten regular tensegrity prisms, each composed of two solid triangular plates (bases), three cross bars, and three cross cables. Bars and bases are additively manufactured in a titanium alloy, through electron-beam melting, while cross cables are made of Spectra fibers and are added to the titanium structure afterward 3D-printing process. The experimental response of the examined tensegrity column under impact loading is studied by recording the waves traveling through the system by means of a Digital Image Correlation algorithm, which measures the axial displacements of the bases of each unit.*

We compare the experimental results with those obtained from numerical simulations performed by adopting two different nonlinear elastic models: one accounting for the presence of bending-stiff connections between the 3D-printed elements, and for the resulting mixed bending-stretching regime; the other one being a tensegrity model which describes a purely stretching response of the column. Such a comparison shows that the presence of bending-stiff connections may weaken the nonlinearity of the wave dynamics that is typical of tensegrity lattices with frictionless nodal connections. We also observe that a marked nonlinear behavior occurs in the case of pure-tensegrity response (no bending deformation) under small prestress.

Peer-review under responsibility of the organizing committee of COMPDYN 2017.
doi: 10.7712/120117.5762.17728

1 INTRODUCTION

In recent years, the dynamics of acoustic metamaterials has been intensively investigated with the aim of designing novel mechanical devices, such as, e.g., acoustic band gap materials, shock protector devices, acoustic lenses, and energy trapping containers, to name just a few examples (refer to [1, 2, 3, 4, 5, 6, 8] and references cited therein for a review). It has been shown that these engineered materials may find application for protecting materials and structures against impacts with external objects [2, 9], as well as for the design of sound-focusing devices and the manufacturing of noninvasive sensors and actuators for structural health monitoring [10, 11, 12, 13].

Special attention are receiving lattice structures obtained by assembling tensegrity units, such as *T3* tensegrity prisms [24], since it has been shown that such systems exhibit a mechanical response that can be continuously varied from hardening to softening, by changing the geometrical, mechanical, and prestress parameters [14, 18, 15, 7]. The geometrically nonlinear response of a tensegrity system is caused by the presence of one ore more *infinitesimal mechnisms*, i.e. sets of nodal displacements causing second-order member elongations, owing to the fact that the equilibrium operator is singular in the considered configuration [16, 17]. The recent studies [6, 7] have revealed that tensegrity columns composed of T3 prisms are suitable for use as acoustic lenses supporting extremely compact solitary waves.

In this work, we experimentally test the dynamic response of a tensegrity column subjected to impact loading, and correspondingly we perform numerical simulations of the examined tests using two different elastic models, respectively described in Refs. [20] and [23]. An additive manufacturing (AM) technique based on Electron Beam Melting (EBM) is employed to build all the elements of the tested structure, except for the cables, which are subsequently added to the 3d-printed structure through a post-tensioning technique [18]. The mechanical modeling of such a structure is first analyzed through the *stick-and-spring* model presented in [20], which takes into account that the nodes of the 3D-printed structure form bending-stiff connections between elements. It models the system by considering bars and bases to be inflexible, describing the cables as linear springs, and attaching angular springs to the nodes (*mixed bending-stretching response*). The second examined model [23] is instead a pure tensegrity model that introduces frictionless pin-connections between elements, describes the cables as linear springs and models the bars and the bases of the prisms as rigid bodies (*purely stretching response* of each cable of the system). Other than comparing for the first time the experimental impact response of a tensegrity column to the numerically predicted response of the above models, this work highlights differences and similarities between such models, providing useful directions for the design of tensegrity metamaterials with sound-focusing abilities.

The paper is organized as follows. Section 2 details the experimental setup and the examined physical model of a tensegrity column. Next, Sects. 3.1–3.3 describe the main features of the stick-and-spring model, while Sect. 3.4 illustrates a comparison between the predictions of such a model and the results of the impact test carried out as described in Sect. 2. A similar comparative analysis is presented in Sect. 4 with reference to the pure tensegrity model. Concluding remarks and directions for future research are drawn in Sect. 5.

2 EXPERIMENTAL SETUP

We experimentally investigated the dynamic response of a 3D-printed physical model of a tensegrity column [22, 7, 18, 23] under impact loading. Such structure consists of ten regular tensegrity prisms with triangular bases (*T3 prisms*) [24, 25] superposed to each other. Figure

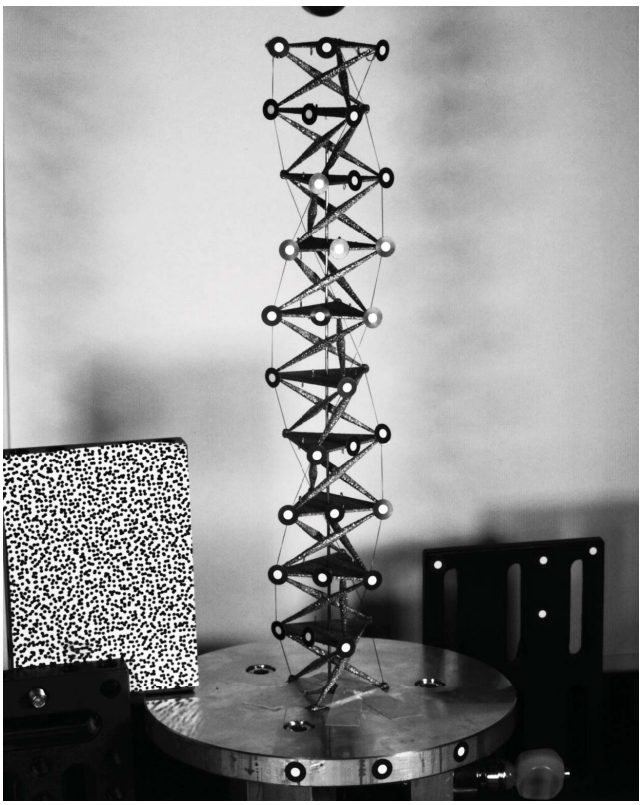

Figure 1: The tensegrity column under test.

1 shows the tested column partly manufactured in Ti6Al4V titanium alloy using the Electron Beam Melting (EBM) technique [18]. The Arcam S12 EBM facility at the Department of Materials Science and Engineering, University of Sheffield was employed to manufacture the examined structure, by depositing layers of Ti6Al4V powder with minimum feature size down to 0.4 mm [19].

Each T3 prism in the column is *left-handed*, i.e. the upper base is rotated counter-clockwise with respect to the bottom base by an angle of $5\pi/6$ about the prism's axis[1] (cf. [23]). Moreover, each T3 prism is made by three bi-conical bars connected to the vertices of two triangular plates of thickness t by means of spherical nodes of 3 mm in diameter. These elements are 3D-printed together with the aid of additional sacrificial linear elements which are mechanically removed afterward. Three strings elements (or *cables*) are then added to each prism on using the post-tension technique illustrated in [18]. The geometric properties of a prism are given in Tab. 1. The symbols s_N, b_N, and h_N denote respectively the length of the edges of the base plates, the length of the bars, and the height of the prism (measured as the distance between the base centers) [18]. The maximum and minimum diameters of the bars are denoted by D and d, respectively.

An in-house experimental setup is designed and assembled to apply an impact load to the top base of the column, while keeping the bottom base fixed to an aluminum plate. The strings of the structure are pre-stretched by passing them through bridge pins applied to the aluminum plate (Fig. 1). In order to maintain the column straight, a vertical thin rod was placed along the column's axis, passing through holes realized on all bases except the last two, and fixed to the aluminum plate.

[1] When a T3 prism is *right-handed* the base is rotated clockwise by the same angle.

t	s_N	b_N	h_N	D	d
(mm)	(mm)	(mm)	(mm)	(mm)	(mm)
1.0	34.08	44.06	22.29	3.0	0.5

Table 1: Geometrical properties of a T3 prism.

The top base is impacted by a spherical striker with mass 5 g made of Polytetrafluoroethylene (PTFE), which falls with null initial velocity for 0.5 m in a duct delimited by four Teflon tubes. The motion of the column produced by the impact with the striker is recorder through two high-speed cameras FASTCAM Mini UX100, and the axial (vertical) displacements of the upper base of each unit are measured using a Digital Image Correlation technique.

3 STICK-AND-SPRING MODEL

3.1 Model description

The AM technique described in section 2 does not allow for the realization of spherical hinges between bars and base plates of the EBM-manufactured tensegrity column; on the contrary, the nodes of the 3d-printed structure provide bending-stiff connections between such elements. Such an observation leads us to employ a stick-and-spring (S&S) model [20] to describe the dynamic response of the phycal model under examination. A S&S structure is a collection of *nodes*, *edges*, and *wedges*: edges are imagined as node-to-node inflexible but extensible straight *sticks*, acting as *axial springs* when extended; wedges are imagined as complexes of two sticks sharing one end node, equipped by a *angular spring* reacting to relative rotations of the two wedge sticks in their common plane. A S&S structure differs from a tensegrity structure because, owing to the presence of angular springs, edges are subjected to shear forces and bending/torsion moments, in addition to axial forces. In the remainder of this section, we summarize the treatment of S&S structures presented in [20].

The combinatorial description of a S&S structure is given by the triplet $\mathcal{S} = (\mathcal{N}, \mathcal{E}, \mathcal{W})$ consisting of: (i) a collection $\mathcal{N}$ of N points, called *nodes*, of the three-dimensional Euclidean space; (ii) a collection $\mathcal{E}$ of E *edges*, that is, two-elements subsets of $\mathcal{N}$; (iii) a collection $\mathcal{W}$ of W *wedges*, that is, three-elements subsets of $\mathcal{N}$. We say that $ij \in \mathcal{E}$ is the edge connecting nodes $i, j \in \mathcal{N}$, and that $ijk \in \mathcal{W}$, with $i, j, k \in \mathcal{N}$, is the wedge with *head node* i and *tail nodes* j and k.

We denote by $\boldsymbol{p}_i$ the *referential position vector* of the typical node i with respect to a chosen origin point, by $\boldsymbol{u}_i$ its displacement, and by $\boldsymbol{q}_i := \boldsymbol{p}_i + \boldsymbol{u}_i$ its *current position vector*. Moreover, we introduce the referential unit vector directed from node i to node j,

$$\boldsymbol{e}_{ij} := \frac{1}{l_{ij}}(\boldsymbol{p}_j - \boldsymbol{p}_i) = -\boldsymbol{e}_{ji}, \tag{1}$$

and the unit vector currently directed from node i to node j,

$$\boldsymbol{c}_{ij} := \frac{1}{\ell_{ij}}(\boldsymbol{q}_j - \boldsymbol{q}_i) = -\boldsymbol{c}_{ji}, \quad \ell_{ij} := |\boldsymbol{q}_j - \boldsymbol{q}_i|, \tag{2}$$

where $l_{ij} := |\boldsymbol{p}_i - \boldsymbol{p}_j|$ is the referential length of edge ij, and ℓ_{ij} its current length.

The strain measures we adopt are:

1. the *change in length* of edge ij:

$$\delta l_{ij} := \ell_{ij} - l_{ij}, \tag{3}$$

2. the *change in angle* of wedge ijk:

$$\delta\theta_{ijk} := \arccos\left(\boldsymbol{c}_{ij}\cdot\boldsymbol{c}_{ik}\right) - \arccos\left(\boldsymbol{e}_{ij}\cdot\boldsymbol{e}_{ik}\right) \tag{4}$$

It is not difficult to see that the linearized strain measure corresponding to (3) and (4) are, respectively:

$$\delta l_{ij} \simeq \varepsilon_{ij} := \boldsymbol{e}_{ji}\cdot\left(\boldsymbol{u}_i - \boldsymbol{u}_j\right), \quad \delta\vartheta_{ijk} \simeq \psi_{ijk} := -\frac{1}{l_{ik}}\,\boldsymbol{w}_{ikj}\cdot\left(\boldsymbol{u}_k - \boldsymbol{u}_i\right) - \frac{1}{l_{ij}}\,\boldsymbol{w}_{ijk}\cdot\left(\boldsymbol{u}_j - \boldsymbol{u}_i\right), \tag{5}$$

with

$$\boldsymbol{w}_{ijk} = \frac{\boldsymbol{P}_{ij}\,\boldsymbol{e}_{ik}}{|\boldsymbol{P}_{ij}\,\boldsymbol{e}_{ik}|} \quad \text{and} \quad \boldsymbol{w}_{ikj} = \frac{\boldsymbol{P}_{ik}\,\boldsymbol{e}_{ij}}{|\boldsymbol{P}_{ik}\,\boldsymbol{e}_{ij}|}, \tag{6}$$

where $\boldsymbol{P}_{ij} := \boldsymbol{I} - \boldsymbol{e}_{ij}\otimes\boldsymbol{e}_{ij}$ and $\boldsymbol{P}_{ik} := \boldsymbol{I} - \boldsymbol{e}_{ik}\otimes\boldsymbol{e}_{ik}$ are the orthogonal projectors on the planes of normal $\boldsymbol{e}_{ij}$ and $\boldsymbol{e}_{ik}$, respectively.

3.2 Compatibility, equilibrium, and constitutive, operators

Let $\boldsymbol{u}$ and $\boldsymbol{\eta}$ denote, respectively, the string of nodal-displacement vectors and the string of strain components:

$$[\boldsymbol{u}] = \left[\ldots, \boldsymbol{u}_i^T, \ldots\right]^T \qquad \text{and} \qquad [\boldsymbol{\eta}] = \left[\ldots, \varepsilon_{ij}, \ldots \,|\, \ldots, \psi_{ijk}, \ldots\right]^T. \tag{7}$$

Then, relations (5) can be written in the following compact form:

$$\boldsymbol{\eta} = \boldsymbol{B}\boldsymbol{u}, \tag{8}$$

where the linear mapping $\boldsymbol{B}$ is called the *kinematic compatibility operator*. We denote by σ_{ij} and τ_{ijk} the stress measures conjugated with ε_{ij} and ψ_{ijk}, respectively. Likewise, let $\boldsymbol{f}$ and $\boldsymbol{\chi}$ denote, respectively, the string of nodal-force vectors and the string of stress components:

$$[\boldsymbol{f}] = \left[\ldots, \boldsymbol{f}_i^T, \ldots\right]^T, \qquad [\boldsymbol{\chi}] = \left[\ldots, \sigma_{ij}, \ldots \,|\, \ldots, \tau_{ijk}, \ldots\right]^T. \tag{9}$$

With this notation, the *balance equations* can be written as

$$\boldsymbol{f} = \boldsymbol{A}\boldsymbol{\chi}, \tag{10}$$

where $\boldsymbol{A} = \boldsymbol{B}^T$ is the formal adjoint of the compatibility operator, termed the *equilibrium operator*. More explicitly, adopting the strain measures (5), it is not difficult to see that (10) is equivalent to:

$$\boldsymbol{f}_i = \sum_{\{j\in\mathcal{N}\,|\,ij\in\mathcal{E}\}} \sigma_{ij}\,\boldsymbol{e}_{ji} + \sum_{\{j,k\in\mathcal{N}\,|\,ijk\in\mathcal{W}\}} \tau_{ijk}\left(\frac{\boldsymbol{w}_{ijk}}{l_{ij}} + \frac{\boldsymbol{w}_{ikj}}{l_{ik}}\right) - \sum_{\{k,j\in\mathcal{N}\,|\,kij\in\mathcal{W}\}} \tau_{kij}\frac{\boldsymbol{w}_{kij}}{l_{ki}}. \tag{11}$$

Next, let the (positive) *stiffness constants* κ_{ij} and λ_{ijk} characterize the linear elastic response of edge and wedge springs:

$$\sigma_{ij} = \kappa_{ij}\,\varepsilon_{ij} \;\text{ and }\; \tau_{ijk} = \lambda_{ijk}\,\psi_{ijk}; \tag{12}$$

we write this set of relations in compact form as:

$$\boldsymbol{\chi} = \boldsymbol{C}\boldsymbol{\eta}, \tag{13}$$

with $\boldsymbol{C}$ is the *constitutive operator*, a diagonal operator whose matrix representation is:

$$[\boldsymbol{C}] = \left[\mathrm{diag}(\cdots, \kappa_{ij}, \cdots \,|\, \cdots, \lambda_{ijk}, \cdots)\right]. \tag{14}$$

3.3 Motion equations

We postulate the following expression for the elastic energy stored in a S&S structure:

$$\mathcal{U} = \frac{1}{2}\Big(\sum_{ij\in\mathcal{E}} \kappa_{ij}(\ell_{ij} - \overline{\ell}_{ij})^2 + \sum_{ijk\in\mathcal{W}} \lambda_{ijk}(\theta_{ijk} - \overline{\theta}_{ijk})^2 \Big)\,, \tag{15}$$

where ℓ_{ij} and $\overline{\ell}_{ij}$ are the current and rest lengths of the axial spring on edge ij, while θ_{ijk} and $\overline{\theta}_{ijk}$ are the current and rest angles of the angular spring on wedge ijk. On introducing the kinetic energy

$$\mathcal{K}(\boldsymbol{q}, \dot{\boldsymbol{q}}) = \frac{1}{2}\, \dot{\boldsymbol{q}} \cdot \boldsymbol{M}(\boldsymbol{q})\dot{\boldsymbol{q}}, \tag{16}$$

with $\boldsymbol{M}$ is a diagonal *mass operator* corresponding to lumped nodal masses, the nonlinear motion equations are given by

$$\boldsymbol{M}\,\ddot{\boldsymbol{q}} + \widetilde{\boldsymbol{A}}(\boldsymbol{q})\boldsymbol{\chi}(\boldsymbol{q}) = \boldsymbol{0}, \tag{17}$$

where $\widetilde{\boldsymbol{A}}(\boldsymbol{q})$ is the *equilibrium operator* in the current placement. This equation can be linearized about an equilibrium placement $\boldsymbol{q}_0$, obtaining:

$$\boldsymbol{M}(\boldsymbol{q}_0)\ddot{\boldsymbol{u}} + \boldsymbol{K}_T(\boldsymbol{q}_0)\boldsymbol{u} = \boldsymbol{0}, \tag{18}$$

where $\boldsymbol{K}_T := \partial^2_{\boldsymbol{q}}\mathcal{U}$ is the *tangent stiffness operator*[2].

The simulation of the column response under impact loading is obtained through numerical integration of (17) and (18) subject to assigned initial conditions.

3.4 Simulation of impact tests

The impact tests described in Sect. 2 were simulated through the S&S model by making use of the following assumptions.

- Cables are modeled as edges, with stiffness $\kappa_c = E_c\pi d_c^2/(4l_c)$, where E_c is the Young modulus, d_c the diameter, and $l_c = \left(l_b^2 - 2\sqrt{3}a^2\right)^{1/2}$ is the current length of the cables, with l_b the length of the bar and a the base radius;
- Cable prestress is considered to be negligible[3];
- Bars are modeled as edges with stiffness $\kappa_b = E_b\pi d_b^2/(4l_b)$, where E_b is the Young modulus and d_b the diameter;
- Each triangular base is modeled as three pin-jointed bars of stiffness κ_b forming the triangle;
- Wedges are considered between base triangles and bars (see Fig. 2, right), their stiffness is $\lambda = \alpha\kappa_b l_c^2$, with α a dimensionless parameter to be fitted with the experimental results;
- Nodal masses m are assigned by subdividing the total measured mass of the structure, 53.0 g into 3 (vertices) $\times$ 10 (bases) = 30 equal parts.

[2] See [20] for a detailed expression of $\boldsymbol{K}_T$.

[3] We checked that, owing to the small axial stiffness of the cable, a modest prestress does not change results significantly.

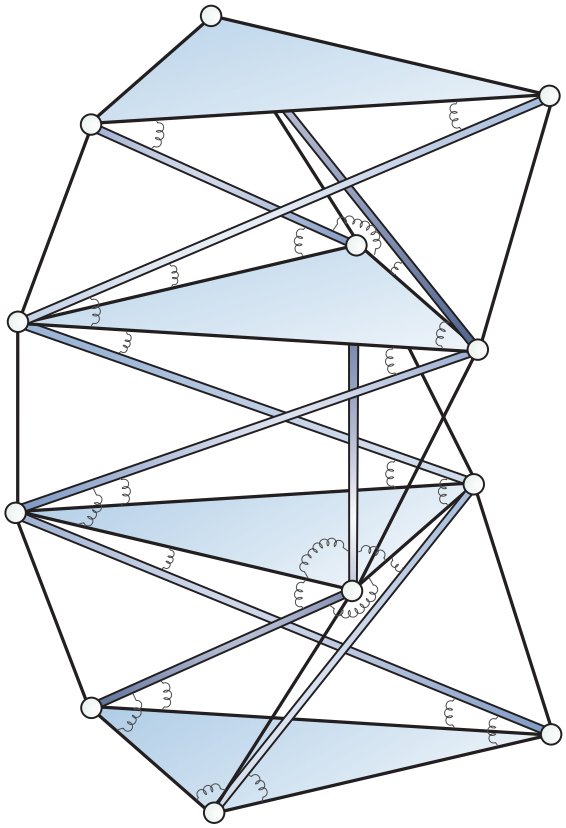

Figure 2: Sketch of a portion of the model showing also the angular springs associated to the wedges of the S&S structure.

- As initial value of the downward velocity we assumed $v_0 = 2\,\text{m/s}$, by averaging measurements during a short time interval after impact. We also assumed that the impact cause the top base to have an initial angular velocity about the prism's axis given by $\omega_0 = 2h_N v_0/a^2 \simeq 0.2304\,\text{rad/s}$, with $a = \sqrt{3}\,s_N/3$, so that the top base initially moves along the infinitesimal mechanism of the top prism [24].

Table 2 summarizes the adopted values of the S&S modeling parameters.

E_c	5480 MPa
d_c	0.1 mm
l_b	44.06 mm
E_b	$110 \cdot 10^3$ MPa
d_b	1.75 mm
h_N	22.29 mm

Table 2: Model parameters.

The stiffness of wedge springs, controlled by the dimensionless parameter α, is assigned by matching the time $\bar{t}$ at which the top base returns to the initial position (subsequently continuing its upward motion). In the experiment, $\bar{t} = 18.9892$ ms; in the simulation, the same value is found when $\alpha = 6.0655 \cdot 10^{-4}$. We observe that by proceeding in this way, a good agreement is found also between oscillation amplitudes in the two cases.

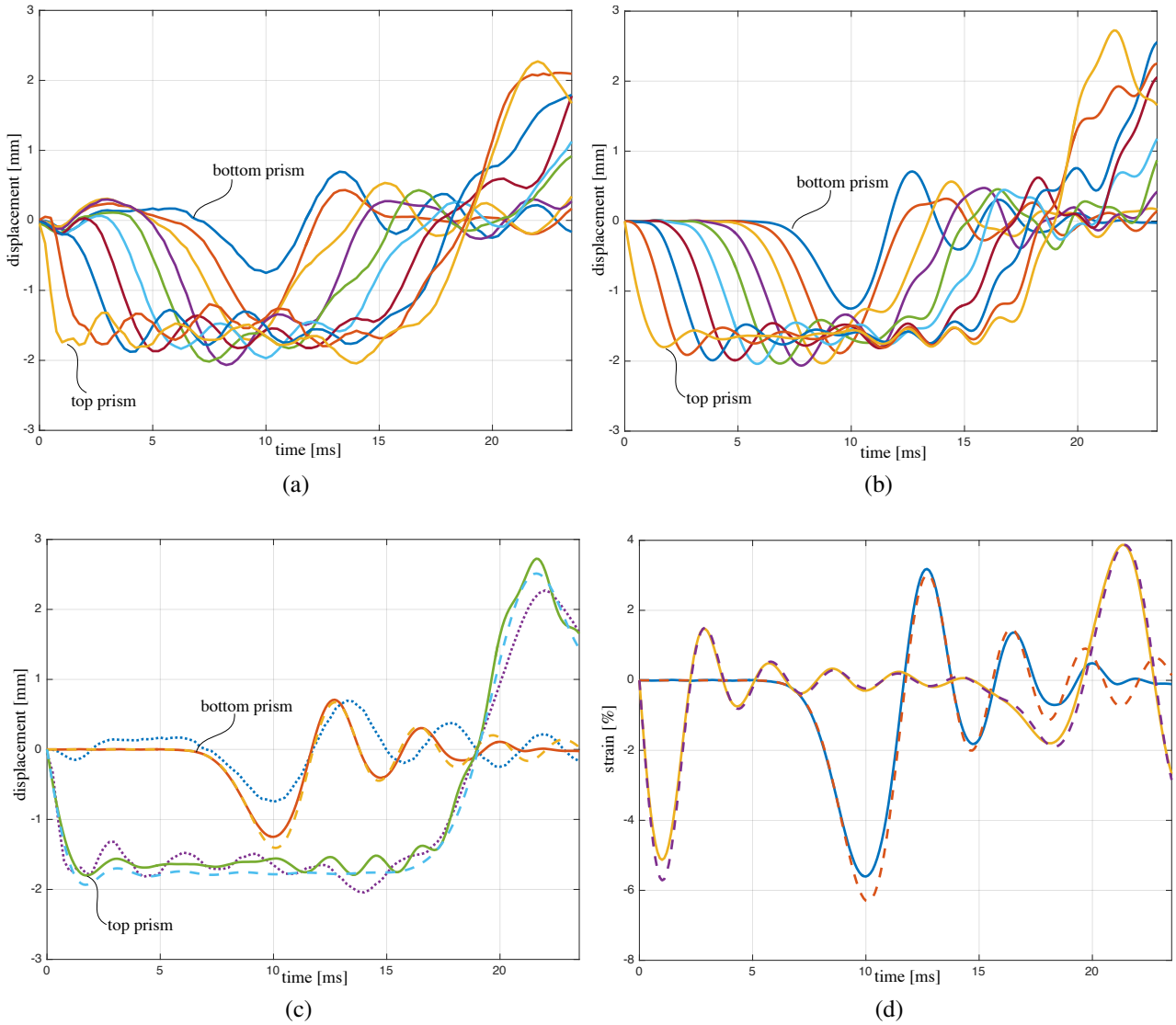

Figure 3: (a) Base displacements obtained from experiments. (b) Base displacements obtained from simulations. (c) Displacements of the top and bottom base, comparison between experiments (dotted line) and numerical simulations with nonlinear theory (solid line) and linearized theory (dashed line). (d) Axial strains in the top and bottom prism obtained with nonlinear theory (solid line) and linearized theory (dashed line).

Fig. 3 (a) shows the displacement of all bases as measured and recorded in the experiment. Fig. 3 (b) shows the displacements obtained by numerical integration of the nonlinear equation of motion (17). Fig. 3 (c) shows a comparison on the displacements of the first and the last prism, between experimental results (dotted line), results obtained by numerical integration of both the nonlinear equation of motion(17) (solid line), and those obtained from the linearized equation of motion(18) (dashed line). Fig. 3 d) shows numerical results for the axial strain of the first and last prism, which is defined as the relative displacement between the two bases of a prism, divided by h_N. Experimental results displays larger oscillations, in particular for the bottom prism. In this regard, we observed that in the experiment triangular bases do not remain perfectly horizontal during the motion, and this is likely to be the reason of the larger oscillations in the measured displacement. The first maximum value of the displacement $u_{\max}$ and the correspondent time $t_{\max}$ is reported in Table (3).

prism	$u_{\max}$ [mm] (exper.)	$u_{\max}$ [mm] (nonlin. th.)	$u_{\max}$ [mm] (lineariz. th.)	$t_{\max}$ [ms] (exper.)	$t_{\max}$ [ms] (nonlin. th.)	$t_{\max}$ [ms] (lineariz. th.)
bottom	-0.7506	-1.2495	-1.4079	10	10	10.1
top	-1.7812	-1.8004	-1.9344	1.75	1.7	1.7

Table 3: First maximum value of the displacement $u_{\max}$ and correspondent time $t_{\max}$.

4 PURE TENSEGRITY MODEL

Both simulations and experimental results presented in the previous section show that the mixed bending-stretching regime produces an essentially linear behavior of the tensegrity column under examination. In this section, we propose some possible directions toward the design of a device with nonlinear behavior in a pure stretching regime. In order to do this, we adopt the simpler, pure tensegrity model presented in [23], where the Lagrange's equation of motion of a tensegrity column are solved numerically. The assumptions of this model are the following ones: only cyclic-symmetric motions with respect to the column's axis are considered; nodes are frictionless hinges between connected elements; all bars are rigid and massless; cables are linearly elastic and massless. In our case, each triangular base is a rigid body with a mass $3\,m$ and moment of inertia $3\,m\,a^2$.
We investigated the following three cases.

CASE 1 — We considered cable stiffness to be the same as in the present S&S model. Then we determined the cable prestrain by matching the time $\bar{t}$ with that of the experiment. By doing so, the resulting prestrain takes the unrealistic value of 85%. The results are shown in Fig. 4 (dashed line) , where it is possible to see a linear behavior similar to that of the mixed bending-stretching response.

CASE 2 — We assign the more realistic value of 5% to the prestrain and determine the cable stiffness by matching the time $\bar{t}$ with that of the experiment. The resulting cable stiffness is 15.5 times higher than that of the original structure. Results are shown in Fig. 4 (dash-dot line), where we still observe a response similar to that of the mixed bending-stretching regime.

CASE 3 — We assign a low prestrain to cables, equal to 1% and, again by matching the time $\bar{t}$ with that of the experiment, we determine the stiffness of cables to be 55.5 times higher than that of the original structure. The results are shown in Fig. 4 (solid line), which displays a much more marked nonlinear response[4].

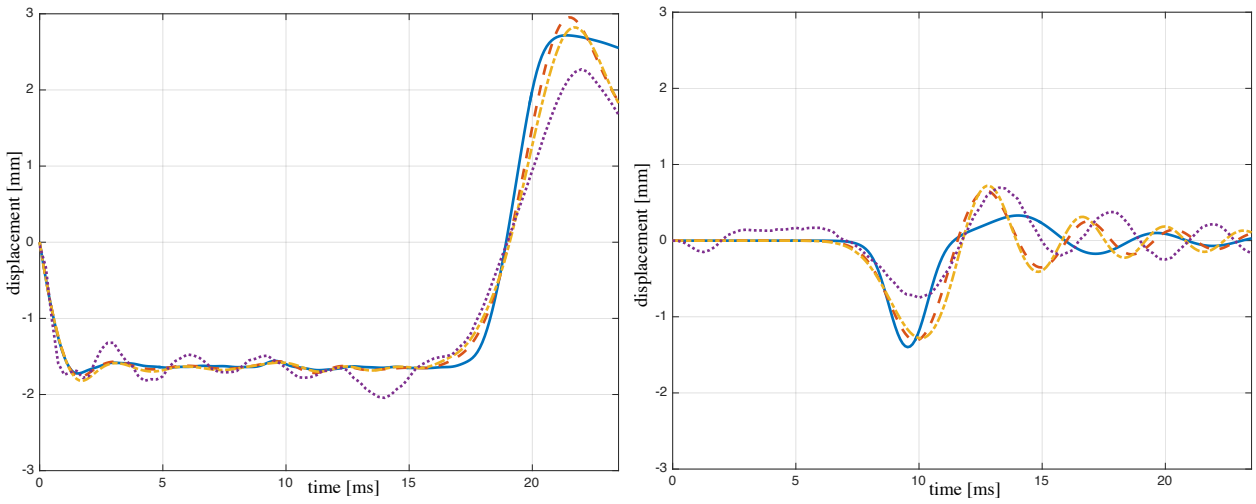

(a) (b)

Figure 4: Displacements of top prism (a) and bottom prism (b): experiments (dotted line), case 1 (dash-dot line), case 2 (dashed line) and case 3 (solid line).

It is worth noting that the above cases refer to models of tensegrity columns different from that experimentally tested in the present work (experimental model), and they are here presented with the aim of exploring the nonlinear potential of the wave dynamics of pure tensegrity lattices. The results in Fig. 4 show that all the analyzed tensegrity models reproduce fairly well the displacement vs. time response of the experimental model. For a better visualization of nonlinear effects, we represented in Fig. 5 the strain of each prism of the column at a fixed time ($t = 6.5$ ms). By comparing Cases 1-3 and the Stick-and-Spring model analyzed in Sect. 3 (nonlinear theory), we observe that for Case 3 (when the cross-cable prestrain is 1%) the deformation of the column is more localized at the wave front.

5 CONCLUDING REMARKS

We have performed an impulsive dynamic test on a physical model of a tensegrity column, on comparing the measured displacements to those computed numerically through two different models: a stick-and spring model accounting for bending deformation of the nodes [20], and a pure tensegrity model accounting for a pure-stretching response of all the members of the system [23]. The first model is intended to capture the experimental response of the analyzed physical model, while the second one is aimed at providing directions for the design of alternative systems featuring highly nonlinear dynamic response. The given results show a fairly good agreement between measurements and simulations performed with the first model. The second model is also able to reproduce the response observed during the experiment by suitably adjusting the stiffness and prestress of cables. We have observed that bending-stiff nodal

[4]This is highlighted for example by the different amplitudes in tension and compression of each prism, owing to a stiffer response in tension, and by a reduced amplitude of the oscillation.

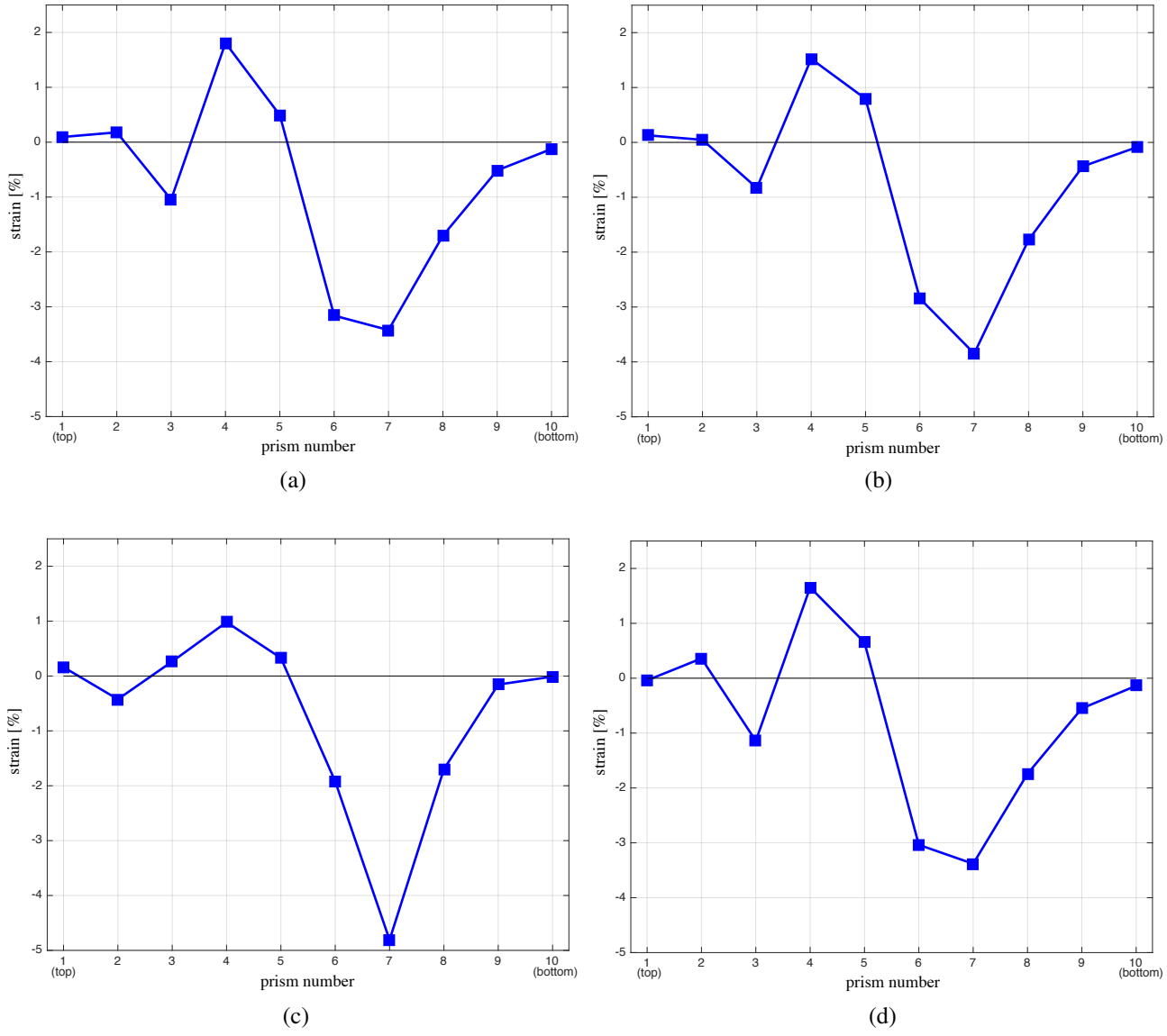

Figure 5: Snapshot at $t = 6.5$ ms of prism strains along the column. Pure tensegrity model: Case 1 (a); Case 2 (b), and Case 3 (c). Nonlinear Stick-and-Spring model (d).

connections, a feature of the 3D-printed structure due to the not-negligible size of the junctions, may greatly reduce nonlinearities in the response of tensegrity lattices. We found that a similar effect can also be obtained in the second model by fictitiously raising the prestress level. This behavior can be explained by considering that the tangent stiffness of the tensegrity lattice is the sum of a material contribution (owing mainly to the stiffness of angular springs) and a geometric contribution (owing to prestress) [20]. In relation to this, we observed also that a more marked nonlinear behavior occurs for smaller prestress levels and smaller values of the stiffness of angular springs.

We are led to conclude that a pure tensegrity behavior with negligible bending deformation of the nodes and low prestress may lead to design novel metamaterials that enable unconventional wavefocusing methodologies based on solitary wave dynamics. This obviously calls for the adoption of manufacturing techniques that are able to build perfect hinges at the nodes, such as, e.g., the multiscale AM tecniques described in [26, 27]. Arrays of tensegrity columns with stretching-dominated response may be employed to fabricate tunable focus acoustic lenses supporting extremely compact solitary waves. On applying different levels of prestress to such metamaterials, one can be able to generate compact solitary waves with different phases within the system, which are expected to interact at a focal point in an adjacent medium (i.e., a material defect to be targeted) [10, 11]. We address specific studies on such engineering applications of tensegrity lattices to future work, with the aim of designing and manufacturing novel acoustic lenses, and innovative sensors/actuators for monitoring structural health and damage detection in materials and structures [10, 11, 12].

Acknowledgements

The authors are grateful to Evert Hernández-Nava, Christopher Smith, Russell Goodall and Ian Smith (Department of Materials Science and Engineering, University of Sheffield, UK) for their precious assistance with the manufacturing of the Ti-6Al-4V experimental model.

REFERENCES

[1] Daraio C., Ngo D., Nesterenko V.F., Fraternali F. (2010) Highly Nonlinear Pulse Splitting and Recombination in a Two Dimensional Granular Network. Phys Rev. E 82:036603.

[2] Fraternali F., Porter M., Daraio C. (2010) Optimal design of composite granular protectors. Mech. Adv. Mat. Struct. 17:1-19.

[3] Leonard A., Fraternali F., Daraio C. (2013) Directional wave propagation in a highly nonlinear square packing of spheres. Exp. Mech. 53(3):327–337.

[4] Nesterenko V.F. (2001) Dynamics of Heterogeneous Materials. Springer-Verlag, New York.

[5] Ngo D., Fraternali F., Daraio C. (2012) Highly Nonlinear Solitary Wave Propagation in Y-Shaped Granular Crystals with Variable Branch Angles. Phys. Rev. E 85(036602):1–10.

[6] Fraternali F., Senatore L., Daraio C. (2012). Solitary waves on tensegrity lattices. J.Mech. Phys. Solids 60:1137–1144.

[7] Fraternali F., Carpentieri G., Amendola A., Skelton R.E., Nesterenko V.F. (2014). Multiscale tunability of solitary wave dynamics in tensegrity metamaterials. Appl. Phys. Lett. 105:201903.

[8] Theocharis G., Boechler N., Daraio C. (2013) Nonlinear phononic structures and metamaterials, in P.A. Deymier (ed.) Acoustic Matematerials and Phononic Crystals, Springer Series in Solid State Sciences, 173.

[9] Mitchell S.J., Pandolfi A., Ortiz M. (2014). Metaconcrete: designed aggregates to enhance dynamic performance. J. Mech. Phys. Solids 65:69–81.

[10] Spadoni A., Daraio C. (2010). Generation and control of sound bullets with a nonlinear acoustic lens. Proc. Natl. Acad. Sci. U.S.A. 107(16):7230–7234.

[11] Donahue C., Anzel P., Bonanomi L., Keller T., Daraio C. (2014). Experimental realization of a nonlinear acoustic lens with a tunable focus. Appl. Phys. Lett. 104:014103.

[12] Ni X. (2011). Nondestructive Evaluation And Structural Health Monitoring Based On Highly Nonlinear Solitary Waves, Phd Dissertation, University of Pittsburgh, USA.

[13] Rizzo P., Ni X., Nassiri S., Vandenbossche J. (2014). A solitary wave-based sensor to monitor the setting of fresh concrete. Sensors 14(7):12568–12584.

[14] Amendola A., Carpentieri G., De Oliveira M., Skelton R.E., Fraternali F. (2014) Experimental investigation of the softening-stiffening response of tensegrity prisms under compressive loading. Compos. Struct. 117:234–243.

[15] Fraternali F., Carpentieri G., Amendola A. (2014). On the mechanical modeling of the extreme softening/stiffening response of axially loaded tensegrity prisms. J. Mech. Phys. Solids, 74:136–157.

[16] Calladine C. R. (1978). Buckminster Fuller's 'tensegrity' structures and Clerk Maxwell's rules for the construction of stiff frames. Int. J. Solids Struct., 14, 161–172

[17] Calladine C. R., Pellegrino S. (1991). First-order infinitesimal mechanisms. Int. J. Solids Struct., 27, 505-515

[18] Amendola A., Hernández-Nava E., Goodall R., Todd I., Skelton R.E., Fraternali, F. (2015). On the additive manufacturing, post-tensioning and testing of bi-material tensegrity structures. Compos. Struct., 131, 66–71.

[19] Tammas-Williams S., Zhao H., Leonard F., Derguti F., Todd I., Prangnell P.B (2015). XCT analysis of the influence of melt strategies on defect population in Ti6Al4V components manufactured by selective electron beam melting. Mater. Charact., 102, 47–61.

[20] Favata A., Micheletti A., Podio-Guidugli P. (2014). A Nonlinear Theory of Prestressed Elastic Stick-and-Spring Structures, International Journal of Engineering Science, 80, 4-20.

[21] Fraternali F., Carpentieri G., Amendola A., 2015. On the mechanical modeling of the extreme softening/stiffening response of axially loaded tensegrity prisms. J.Mech. Phys. Solids, 74, 136–157.

[22] Fraternali F., Senatore L., Daraio C. (2012). Solitary waves on tensegrity lattices. J.Mech. Phys. Solids, 60, 1137-1144.

[23] Davini C., Micheletti A., Podio-Guidugli P. (2016). On the impulsive dynamics of T3 tensegrity chains. Meccanica, 51 (11), 2763-2776.

[24] Oppenheim I, Williams W (2000). Geometric effects in an elastic tensegrity structure. J. Elast. 59:51–65.

[25] Skelton R.E., de Oliveira M.C. (2010). *Tensegrity system*s. Springer, Berlin.

[26] Zheng X. , Lee H. , Weisgraber T.H., Shusteff M., DeOtte J., Duoss E.B., Kuntz J.D., Biener M.M., Ge Q., Q. Jackson J.A., Kucheyev S.O., Fang N.X., Spadaccini C.M. (2014). Ultralight, ultrastiff mechanical metamaterials, Science, 344 (6190) 1373-1377.

[27] Meza L.R., Das S., Greer J.R. (2014). Strong, lightweight, and recoverable three-dimensional ceramic nanolattices, Science, 345 (6202) 1322-1326.